PCCP

Spin Controlled Surface Chemistry: Alkyl Desorption from Si(100)-2x1 by Nonadiabatic Hydrogen Elimination

Journal:	*Physical Chemistry Chemical Physics*
Manuscript ID	CP-ART-04-2020-001913.R2
Article Type:	Paper
Date Submitted by the Author:	02-Jul-2020
Complete List of Authors:	Pohlman, Andrew; University of Nevada Reno, Department of Chemistry Kaliakin, Danil; University of Nevada Reno, Department of Chemistry Varganov, Sergey; University of Nevada Reno, Department of Chemistry Casey, Sean; University of Nevada Reno, Department of Chemistry

ARTICLE

Spin Controlled Surface Chemistry: Alkyl Desorption from Si(100)-2×1 by Nonadiabatic Hydrogen Elimination†

Received 00th January 20xx,
Accepted 00th January 20xx

DOI: 10.1039/x0xx00000x

Andrew J. Pohlman, Danil S. Kaliakin, Sergey A. Varganov, and Sean M. Casey*

An understanding of the role that spin states play in semiconductor surface chemical reactions is currently limited. Herein, we provide evidence of a nonadiabatic reaction involving a localized singlet to triplet thermal excitation of the Si(100) surface dimer dangling bond. By comparing the β-hydrogen elimination kinetics of ethyl adsorbates probed by thermal desorption experiments to electronic structure calculation results, we determined that a coverage-dependent change in mechanism occurs. At low coverage, a nonadiabatic, inter-dimer mechanism is dominant, while adiabatic mechanisms become dominant at higher coverage. Computational results indicate that the spin crossover is rapid near room temperature and the nonadiabatic path is accelerated by a barrier that is 40 kJ/mol less than the adiabatic path. Simulated thermal desorption reactions using nonadiabatic transition state theory (NA-TST) for the surface dimer intersystem crossing are in close agreement with experimental observations.

Introduction

There has been intense recent interest in controlling the behavior of dangling bonds and their resulting electron spins on semiconductor surfaces. Much of this work has been driven by the desire to produce nanoscopic electronic circuit models[1–5] or controllable nanomagnetic domains.[6,7] The majority of these studies focused on cryogenically cooled hydrogen-terminated silicon surfaces and intentionally generated hydrogen vacancies to create surface dangling bonds containing the unpaired electrons.[1] On the Si(100)-(2×1):H surface, electronic coupling into rudimentary circuit component behavior was observed in scanning tunneling spectroscopic (STS) studies of dangling bond states spaced by two or more surface unit cells, either along or across the silicon dimer rows.[2–5] On Si(111)-(7×7), hydrogen atom adsorption on the silicon surface rest atom or adatom positions has been computationally predicted to ferrimagnetically align the dangling bonds on nearby unit cell adatom positions.[6] In a related study, cobalt atoms adsorbed on Si(100), studied by scanning tunneling microscopy (STM) and density functional theory (DFT), display spin magnetic moments having differing magnitudes parallel and perpendicular to the dimer row direction, and this was suggested to contribute to the preferential tip induced motion of the cobalt atoms along the dimer row rather than perpendicular to it.[7] Results from these previous low temperature studies thus suggest that the spin state of surface atoms can exert an influence on the chemistry of neighboring silicon surface atoms. In this paper, we show that this influence can manifest itself at higher temperatures during hydrogen transfer reactions on Si(100) surfaces.

The local excitation of a Si(100) surface dimer is conceptualized in **Scheme 1**, where excitation of the dangling bonds at the surface is required to break up the spin-coupled dangling bond π state and form the dual dangling bond π* state. On a localized level, this excited dimer could be in either a singlet or triplet electronic state.[8] Previous electronic structure studies have suggested that Si(100) surface dimers have thermally accessible triplet excited states that may take part in chemical reactions, but experimental evidence of this has been indirect to date.[9,10] Previous experiments have shown an onset to silicon surface metallization starting in the 400 – 600 K range by showing a temperature dependent population of the π* surface state with the dimer surface reconstruction being conserved.[11–14] Jeon *et al*. implicated the filling of the surface π* state as due to the formation of surface adatoms, for which they supported their argument by reacting an 800 K surface with oxygen, a ground state triplet.[14] They showed through spectroscopic experiments that the π* surface excited state preferentially reacted with oxygen compared to the surface ground state. This would make chemical sense in that the reaction with triplet ground state oxygen would become more facile after a surface dimer converts to a localized triplet by thermal excitation.[15] The energy barrier to the minimum energy crossing point (MECP) for a transition to the triplet state was previously determined to be low enough to suggest that non-negligible populations of the triplet state may be present at and above room temperature.[9,10] Additional theoretical work has shown that when the surface dimers become more symmetrical in their rocking angle or when the dimers are strained at higher temperatures, the energy gap between the electronic surface

Department of Chemistry and Chemical Physics Program, University of Nevada, Reno, 1664 N. Virginia Street, Reno, Nevada 89557-0216, United States
Email: scasey@unr.edu

†Electronic Supplementary Information (ESI) available: Details for TPD experiments; methods for calculating MECP crossing rate constants; DFT hydrogen elimination transition state geometries; elimination Path 2 IRC calculations; canonical crossing probabilities; parameters for calculating MECP crossing rates; experimental vs. DFT results for ethylene desorption. See DOI: 10.1039/x0xx00000x

band states (π-π^*) decreases.[16,17] These previous studies all suggest that nonadiabatic effects due to the dimer excited state(s) should begin to manifest themselves in Si(100) surface chemistry above room temperature.

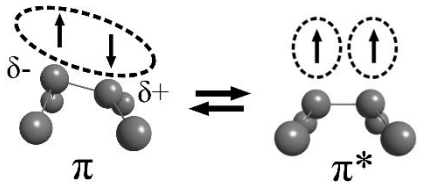

Scheme 1: Si(100) surface dimer singlet to triplet excitation.

The system chosen in order to probe these potential nonadiabatic silicon surface effects was hydrogen transfer reactions from alkyl (specifically, ethyl) groups. Nonadiabatic spin-crossings have been invoked to explain accelerated alkyl hydrogen elimination reactions in solution-phase organometallic reaction mechanisms.[18] This happens due to a lowering of the effective activation barriers in the case of some first-row transition metal complexes. In many of these cases, the spin crossing occurs before the elimination step.[19,20] These nonadiabatic reaction paths have also been described as having two-state or multi-state reactivity.[21] Hydrogen elimination reactions have also been shown to occur on Si(100) and it has been previously demonstrated through isotopic labeling studies that a surface ethyl group will selectively eliminate a hydrogen from the β position, relative to the surface dimer atom, in its decomposition reaction to form the observed ethylene desorption product, as illustrated below in **Scheme 2**.[22,23] An infrared (IR) spectroscopy study showed that the eliminated hydrogen is transferred directly to a silicon surface atom, although the location of the target silicon atom (intradimer versus neighboring surface dimer) was not identified.[24] The occurrence of nonadiabatic hydrogen elimination reaction channels in systems with highly correlated electrons and electronic spin states, such as first row organometallics, suggests that similar kinetics may be observed on the correlated silicon surface and calls for a careful re-examination of the hydrogen elimination reaction on Si(100).

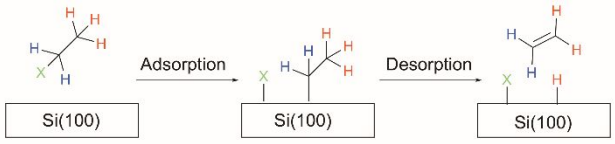

Scheme 2: Thermally-driven hydrogen-elimination desorption reaction of ethyl (C_2H_5) on Si(100), formed after adsorption of ethyl halide, and cleavage of the halogen (green X). A hydrogen atom is eliminated from the β position (red) of the alkyl relative to the surface, forming the ethylene (C_2H_4) desorption product.

Experimental and computational methods

In order to probe potential nonadiabatic effects in the hydrogen elimination reaction on silicon, experiments were performed using a clean, *p*-type Si(100) surface held at 340 K under ultrahigh vacuum (UHV) conditions. The *p*-type silicon wafer (Virginia Semiconductor, 10-15 Ω·cm, boron doped, 25.4 mm diameter, 254 μm thickness) was radiatively heated with the unpolished side facing the tungsten heating elements. The sample temperature was monitored using a type-C thermocouple (W-5%Re vs. W-26%Re) clamped to the polished surface using tantalum foil (ESPI Metals, 0.15 mm thickness, 99.98% purity). The non-linear heating ramp was calibrated against known desorption temperatures for *cis*-2-butene,[25] ammonia,[26] and the desorption products of H_2 and SiO from water adsorption.[27] The sample was exposed to chloroethane (C_2H_5Cl) vapor by backfilling the chamber. Prior to exposure of chloroethane (Aldrich, ≥ 99.7%) via a molecular leak valve, the sample was cleaned by multiple cycles of Ar^+ sputtering and annealing to 1200 K *in situ*. Relative exposures are reported in Langmuir (1 L = 1×10^{-6} torr·s) and were obtained using readings from a nude ion gauge located in the UHV chamber. The orifice to the quadrupole mass spectrometer (QMS) was oriented normal to the sample surface and positioned 2 mm away. During temperature programmed desorption (TPD) experiments the QMS ionization energy was set to 70 eV. Using TPD experiments, reaction products desorbing from the surface were monitored using the QMS as the sample was heated, for a range of relative chloroethane exposures up to the surface saturation level. Additional experimental details can be found in the Supporting Information (**SI**).

Electronic structure calculations were used to explore the possible hydrogen elimination reaction channels. The surface of Si(100) was simulated using a double-dimer row cluster model with stoichiometry $Si_{15}H_{16}$. This model (pictured in the **SI**) has "bulk" silicon dangling bonds terminated with hydrogens, leaving two unterminated silicon dimers as the reactive surface model adsorption sites, and has been commonly used to model Si(100) surface chemical reactivity.[28,29] Minima, transition states (TS), and MECP geometries were optimized using unrestricted density functional theory (U-DFT) with the B3LYP functional[30–32] and the def2-SVP basis set.[33,34] The relative energetics were refined by performing single point energy calculations at minima, TS, and MECP with the larger def2-TZVP basis set.[33,34] Reported energies include zero-point corrections. Computational accuracy was further improved upon by carrying out second-order unrestricted Møller-Plesset perturbation theory (U-MP2) calculations with the def2-TZVP basis set for important reaction barriers.[35] Important barriers were also examined using U-DFT with a larger, triple-dimer row cluster model with stoichiometry $Si_{20}H_{21}$ (see the **SI**). Electronic structure calculations were performed with the General Atomic and Molecular Structure System (GAMESS) package.[36]

Results and discussion

In experimental TPD traces, the desorbing ethylene (C_2H_4) product was selectively measured by monitoring its most abundant *m/z* 27 electron-impact cracking fragment. As shown in **Figure 1A**, the peak desorption temperature, T_P, shifts from 640 K to 540 K as a function of chloroethane exposure, which is in good agreement with previous reports.[22–24] For comparison, in a separate experiment, a clean, 340 K *p*-type Si(100) sample was also exposed to ethylene by backfilling and its *m/z* 27

electron-impact cracking fragment was selectively monitored during TPD experiments, as shown in **Figure 1B**. By comparing the two families of desorption traces (**Fig. 1A** vs. **1B**), one can see that there are significant differences in the desorption mechanism despite the same chemical product desorbing. Ethylene is known to undergo a cycloreversion reaction which produces a narrow TPD peak with very little peak temperature shifting (**Fig. 1B**).[37] However, ethylene produced from surface ethyl groups via β-hydrogen elimination (**Fig. 1A**) has broadened peaks that shift to lower temperatures at higher exposures.

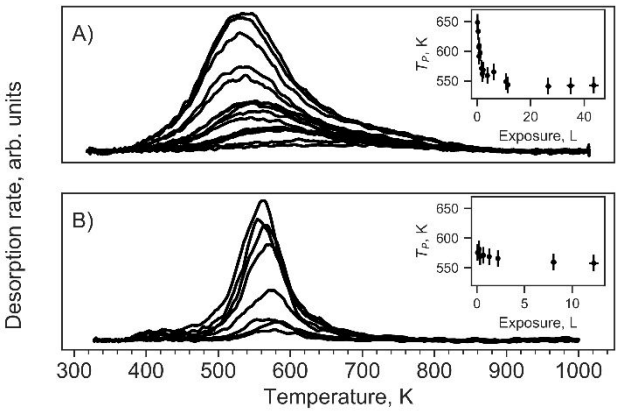

Figure 1: Ethylene desorption while monitoring *m/z* 27 following A) chloroethane and B) ethylene adsorption with peak maximum positions, T_P, as insets. Desorption traces share a common temperature axis.

When the activation energies to desorption, E_{des}, are calculated using the Redhead method[38] for the range of observed experimental peak temperatures from the β-hydrogen elimination reaction, values of 135 – 160 kJ mol^{-1} are obtained, assuming a pre-exponential factor of 1×10^{13} s^{-1}. In a similar fashion, values of 140 – 145 kJ mol^{-1} are obtained for the desorption of ethylene by cycloreversion. While the ethylene cycloreversion E_{des} values are in good agreement with previous experiments,[37] the hydrogen elimination E_{des} values span a large energetic range, indicating the presence of either strong adsorbate-adsorbate interactions or multiple desorption pathways.

To more fully characterize these desorption reactions, electronic structure calculations were used to explore the possible hydrogen elimination reaction channels. Initial adsorbate configurations for computational probing were based on previous experimental STM observations, where it was shown that the adsorption reaction of simple halogenated alkanes preferentially propagates across surface dimer rows.[39,40] Transition states for hydrogen elimination channels were determined, considering intra- (Path 1) and inter-dimer (Paths 2-4) paths within the same dimer row for eliminations from the β position of a surface-bound ethyl, as illustrated in **Figure 2**. Elimination across the trench to a neighboring dimer row is unlikely due to the lack of adjacent unoccupied dimer sites after alkyl halide adsorption, which preferentially occurs across the trench between the dimer rows.[39,40] The calculated transition state geometries of the β-hydrogen elimination on Si(100) are similar to those found in the organometallic literature[18] in that the surface ethyl moiety adopts a *syn*-coplanar geometry, as shown in the **SI**.

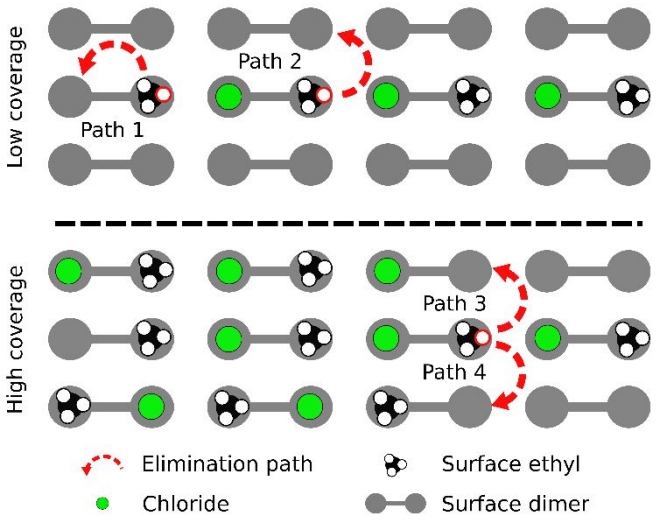

Figure 2: Possible hydrogen elimination channels for ethyl groups on the Si(100) surface are mapped at low (upper panel) and high (lower panel) coverage. Adsorbate configuration pattern is based on STM observations.[39,40]

Elimination mechanisms requiring a spin change were also considered for Path 2, where an empty, adjacent surface dimer is potentially involved in the reaction. A schematic of the critical points for the hydrogen elimination on the singlet versus triplet potential energy surface (PES) for Path 2 is shown in **Figure 3**. Transition states on the lowest energy singlet and triplet state PESs for the cluster models were located. For the Path 2 case where the β hydrogen is eliminated to a neighboring unoccupied dimer, the reaction with a spin-crossing to the triplet state (π*) resulted in kinetically more favorable barrier heights compared to the singlet (π) surface reaction. Intrinsic reaction coordinate (IRC) calculations along elimination Path 2 highlight the differences in energy for the two spin states, revealing a relatively early point of state crossing along the minimum energy paths (**SI**). Indeed, a MECP geometry search between the two spin multiplicities using the IRC intersection as an initial guess confirms that the barrier from the singlet minimum to the MECP is relatively low and is consistent with values reported previously by the Materer group.[10] The presence of a local minimum on the triplet potential energy surface (PES) elimination pathway was also revealed.

It should be noted that a transition state with an open-shell singlet character could be an alternative to a triplet pathway.[41–47] This reaction path would still involve an excitation of the neighboring "acceptor" silicon dimer π to π* state, and a crossing to a different electron configuration at some point during the reaction. The computational methods (U-DFT and U-MP2) described above are unlikely to be able to produce

reliable values for such a pathway (see **SI**), and computations incorporating higher level multireference character are likely to be required.[48] Nonetheless, as will be discussed below, the triplet pathway appears to provide qualitative agreement with TPD experimental data and will be the focus of this analysis.

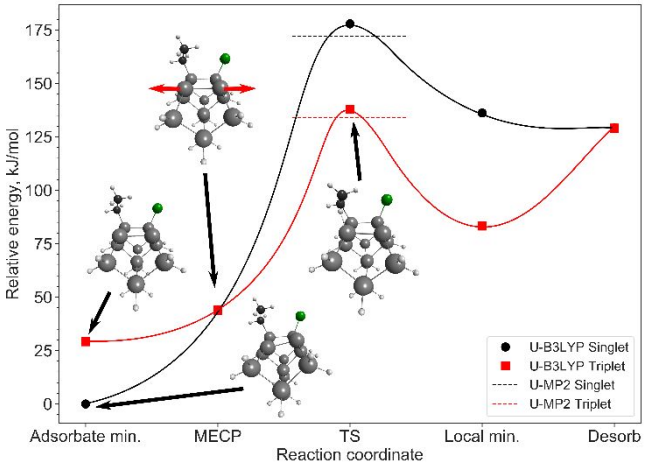

Figure 3: A schematic of the elimination profile for Path 2 including the MECP energy and desorbed state. Optimized structures for critical points are also shown, featuring the conformation of the acceptor dimer in all cases. The vibrational stretch responsible for the crossing is shown for the MECP geometry.

Calculated activation energies, E_a, for the β-hydrogen elimination step of each path are summarized in **Table 1**, while the ratio of the transition state and reactant total partition functions, $Q^{\ddagger}/Q_r$, according to canonical transition state theory, are all within about an order of magnitude of one another and are given in the **SI**. U-MP2 calculations predict similar TS and MECP barriers to those obtained with U-B3LYP. In addition, the calculations performed on the larger cluster model with three Si-Si dimers predicted similar barriers (see the **SI**). In the low coverage regime, it should be noted that elimination Path 1 stems from a minority adsorbate configuration. As previous STM observations have shown, the adsorbate configuration necessary for Path 1 would occur on the terminal ends of the linear propagation for the surface adsorption reaction, while those for Path 2 would make up most of the adsorbed species.[39,40]

Table 1: Summary of the β-hydrogen elimination activation energies, E_a, for reaction paths shown in Figure 2. Energy values were calculated at the U-B3LYP/def2-TZVP level of theory and are zero-point corrected. Values in bold correspond to nonadiabatic mechanisms. DB = dangling bond.

Coverage regime	Path	Nature of the Si atom "receiving" the H	E_a (kJ/mol)
Low	1 (minority species)	DB	126.8
	2 (majority species)	π	178.0
	2 (majority species)	**π***	**137.9**
High	3	DB	113.6
	4	DB	114.1

To compare rates from possible hydrogen elimination channels, temperature-dependent Landau-Zener spin crossing probabilities (P_{LZ}) and canonical rate constants were calculated using NA-TST.[49] The spin-orbit coupling (SOC) constant at the MECP was calculated as a root-mean-square value over the three SOC elements corresponding to the triplet M_S components[49,50] using multiconfigurational quasidegenerate second-order perturbation theory (MCQDPT2).[51,52] The zero-order wave function for MCQDPT2 calculations was of the complete active space self-consistent field (CASSCF(2,2)) type with two electrons in the highest occupied molecular orbital (HOMO) in the singlet state, and with two electrons in the singly occupied molecular orbitals (SOMO) in the triplet state.[53,54] Across the desorption peak temperature range, P_{LZ} ranges were found to be 0.7-0.8%, with a SOC constant of 10 cm^{-1} (**SI**). By comparing the calculated forward and reverse canonical rate constants through the MECP for spin-forbidden crossings, it can be seen that the surface dimer "receiving" the eliminated hydrogen approaches spin equilibrium conditions near the desorption temperatures observed for hydrogen elimination and transitions to a mostly triplet state surface phase at higher temperatures in **Figure 4**. The P_{LZ}-based canonical rate constants for the MECP crossing are 8 – 10 orders of magnitude higher than the rate constants for traversing the calculated hydrogen elimination kinetic barriers at temperatures in the range of the experimentally observed peaks**,** assuming an Arrhenius relationship for the kinetic parameters in **Table 1** and in the **SI**, indicating that it is unlikely that the spin-crossing is rate-limiting.

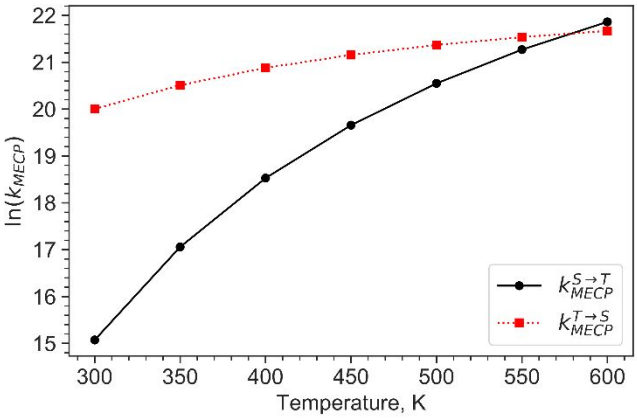

Figure 4: Forward and reverse canonical rate constants for spin-forbidden crossings through the MECP.

To gain more insight into the dimer motion responsible for the spin crossing, a vibrational analysis of the MECP geometry was performed using the effective Hessian.[49,55] The dimer stretch was found to be the primary vibrational mode for the spin crossing at the MECP, shown above in **Figure 3**. Analysis of the energy gradients of the singlet and triplet PESs at the MECP indicates a sloped intersection between the PESs (**SI**). The narrowing of the gap between the surface ground and excited states, the π-π* transition in this case, due to changes in the surface dimer length and conformation, is consistent with previous studies.[16,17] Previous molecular dynamics (MD) simulations of the Si(100) surface at temperatures similar to the observed desorption range produced larger numbers of

strained, symmetric dimers.[16] Additionally, previous band structure calculations comparing buckled and symmetric dimer configurations resulted in a decrease in the gap between occupied and unoccupied surface states in the symmetric dimer case.[17]

To show a more concrete relationship to the experimental data, TPD traces were numerically simulated using the kinetic parameters obtained from the electronic structure calculations for each proposed reaction channel. This was done using the Polanyi-Wigner desorption equation, **Equation 1**, where the desorption rate is dependent on coverage, θ, with a pre-exponential factor ν and order of reaction *n* for a given heating rate, β.

$$-\frac{d\theta}{dT} = \frac{\nu}{\beta}\theta^n e^{-E_a/k_B T} \qquad (1)$$

The calculated traces for each path are compared to experimental TPD traces from low and high coverages, relative to saturation, in **Figure 5**. It should be emphasized here that despite the differences in each path, the same ethylene desorption product will be observed. Since the calculated canonical rates of passage through the MECP are many orders of magnitude more rapid than any of the rates for elimination, it is assumed that an unoccupied acceptor dimer singlet-to-triplet thermal transition is a rapid equilibrium occurring before the elimination step at temperatures comparable to the observed experimental desorption range. When calculating the nonadiabatic, inter-dimer path, an entire surface of dimers occupied as in the case for Path 2 was assumed, where a surface ethyl is always occurring next to an unoccupied acceptor dimer, such that the coverage of the ethyl adsorbate, θ_{Et}, was equal to the coverage of singlet dimer acceptors, θ_{SD}. The relative coverage of triplet acceptor dimers, θ_{TD}, was approximated in **Equation 2** by calculating a temperature-dependent equilibrium constant, *K(T)*, from the P_{LZ}-based forward and reverse rates through the MECP. The overall nonadiabatic desorption rate was calculated in **Equation 3** by using the rate constant derived from the activation energy and pre-exponential factor for a singlet reactant and triplet transition state, k_{elim}.

$$\theta_{TD}(T) = K(T)\theta_{SD} \qquad (2)$$

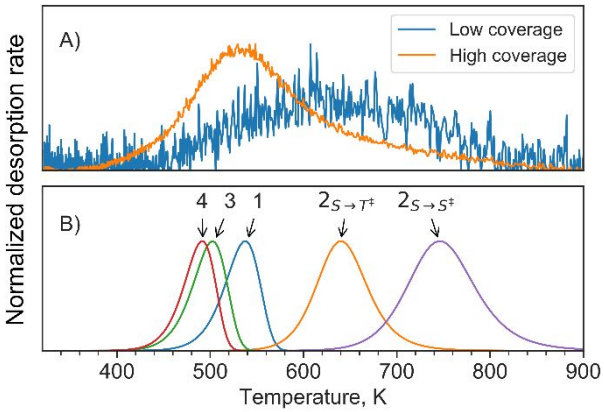

$$rate = k_{elim}\theta_{Et}\theta_{TD} \qquad (3)$$

Figure 5: A comparison of the experimental TPD traces from the β-hydrogen elimination at high and low coverages of chloroethane shown in A) and the simulated TPD traces for each of the presented reaction channels shown in B). Each simulated TPD trace is independently calculated. Plots share a common temperature axis. A comparison of peak position for the adiabatic ($S \rightarrow S^{\ddagger}$) and nonadiabatic ($S \rightarrow T^{\ddagger}$) cases is given for Path 2.

Calculated desorption peaks that cluster in the lower temperature region of the experimental trace correspond to the mechanisms that involve hydrogen eliminations to partially occupied dimers (dangling bond states), such as an intra-dimer mechanism (Path 1) or elimination to a dimer that is already half-occupied (Paths 3 and 4). Mechanisms where the hydrogen is eliminated to a neighboring unoccupied dimer (Path 2), however, tend to produce peaks that are in the higher temperature region of the experimental trace. When the TPD trace for the nonadiabatic, inter-dimer elimination path (Path 2) is calculated, including the Landau-Zener crossing probability, there is close agreement with the experimental peak position for low coverage cases. Traces calculated from adiabatic, inter-dimer pathways produce peaks that are beyond the range of the observed experimental desorption peaks. Thus, the peak desorption temperature shifts can be viewed as being due to a change of desorption mechanism between two coverage regimes. At low coverages, a neighboring acceptor dimer is more likely to be completely unoccupied and will require a crossover to the π* excited state before the elimination reaction can initiate the desorption process. At higher coverages, an acceptor dimer is more likely to be partially occupied and the state-crossing requirement is not necessary for those desorption channels.

The broadened desorption peak from the β-hydrogen elimination desorption mechanism is due to these multiple possible reaction channels and this visibly contrasts with the cycloreversion mechanism for ethylene desorption, as shown above in **Figure 1**, which would desorb through a single channel. Electronic structure calculations were also performed to model the desorption pathway of ethylene cycloreversion. Theoretical TPD traces for ethylene desorption were numerically simulated according to **Equation 1**. There is close agreement for the desorption peak position when comparing the experimental ethylene trace to the DFT-derived results (**SI**), and the experimental peak position is observed to be in close

agreement with previous reports.[37] There is a slight mismatch when comparing the experimental to the calculated peak widths, which can be attributed to some degree of nonhomogeneous sample heating. When considering the experimental broadening of the ethylene desorption peak width compared to its theoretical trace, differing only by a factor of 1.5 – 2 in the case of the cycloreversion reaction, it becomes more apparent that the broad peak corresponding to β-hydrogen elimination desorption is a result of several convoluted paths, including the initial low-coverage nonadiabatic elimination reaction channel.

Conclusions

To conclude, through a combination of experimental TPD studies, electronic structure calculations, and application of NA-TST, it has been demonstrated that the β-hydrogen elimination desorption mechanism for ethyl groups on the Si(100) surface is a coverage-dependent process that produces the same observed desorption product through several convoluted reaction channels. This is in contrast with the cycloreversion of adsorbed ethylene, which appears to desorb via one reaction channel. Good agreement is obtained when comparing results from electronic structure calculations on cluster models for individual ethyl desorption channels to the experimental TPD traces across a range of coverages. In the low coverage regime, a nonadiabatic, inter-dimer mechanism is dominant (Path 2) and relies on a thermally driven excitation to produce a neighboring π^* acceptor dimer to initiate the hydrogen elimination reaction leading to desorption. A model based on NA-TST kinetics closely reproduces the desorption peak position for this spin-controlled desorption channel. At higher coverages, the weak π system of the acceptor dimer is broken by the presence of another surface species, producing reactive, uncoupled dangling bond electrons, which undergo facile hydrogen elimination reactions. The importance of the surface dimer stretching mode was highlighted as a major contributor to the singlet to triplet excitation process. We believe that this or similar spin-coupled, nonadiabatic reaction paths are likely to become increasingly important at temperatures above room temperature on silicon surfaces. While NA-TST with the simple Landau-Zener transition probability treatment appears to be adequate for explaining the reported experimental findings, it would be interesting to investigate the effects of quantum tunneling[55] and multidimensional dynamics[56–59] in nonadiabatic reactions on silicon surfaces.

Conflicts of interest

There are no conflicts to declare.

Acknowledgements

This work was supported by the National Science Foundation (NSF) through a CAREER Award (CHE-1654547) to S.A.V. We thank Dr. Aleksandr Lykhin for providing a script for calculating an effective Hessian at the MECP.

Notes and references

1 S. R. Schofield, P. Studer, C. F. Hirjibehedin, N. J. Curson, G. Aeppli, D. R. Bowler, *Nat. Commun.* **2013**, *4*, 1649.
2 M. Yengui, E. Duverger, P. Sonnet, D. Riedel, *Nat. Commun.* **2017**, *8*, 1.
3 T. Huff, H. Labidi, M. Rashidi, L. Livadaru, T. Dienel, R. Achal, W. Vine, J. Pitters, R. A. Wolkow, *Nat. Electron.* **2018**, *1*, 636.
4 M. Rashidi, W. Vine, T. Dienel, L. Livadaru, J. Retallick, T. Huff, K. Walus, R. A. Wolkow, *Phys. Rev. Lett.* **2018**, *121*, 166801.
5 M. Rashidi, R. Achal, L. Livadaru, J. Croshaw, R. A. Wolkow, *ACS Nano* **2019**, *13*, 10566.
6 X.-Y. Ren, C.-Y. Niu, S. Yi, S. Li, J.-H. Cho, *Phys. Rev. B* **2018**, *98*, 195424.
7 M. Yengui, E. Duverger, P. Sonnet, D. Riedel, *J. Phys. Chem. C* **2019**, *123*, 26415.
8 N. A. Besley, A. J. Blundy, *J. Phys. Chem. B* **2006**, *110*, 1701.
9 J. S. Hess, D. J. Doren, *J. Phys. Chem. B* **2002**, *106*, 8206.
10 Q. Zhu, N. F. Materer, *Chem. Phys. Lett.* **2010**, *496*, 270.
11 L. Gavioli, M. G. Betti, C. Mariani, *Phys. Rev. Lett.* **1996**, *77*, 3869.
12 C. C. Hwang, T.-H. Kang, K. J. Kim, B. Kim, Y. Chung, C.-Y. Park, *Phys. Rev. B* **2001**, *64*, 201304.
13 P. Eriksson, M. Adell, K. Sakamoto, R. Uhrberg, *Phys. Rev. B* **2008**, *77*, 085406.
14 C. Jeon, C. C. Hwang, T.-H. Kang, K.-J. Kim, B. Kim, Y. Kim, D. Y. Noh, C.-Y. Park, *Phys. Rev. B* **2009**, *80*, 153306.
15 T.-R. Kim, S. Shin, C. H. Choi, *J. Chem. Phys.* **2012**, *136*, 214704.
16 B. C. Pan, H. Y. He, *Phys. Rev. B* **2008**, *77*, 113302.
17 J.-H. Cho, J.-Y. Lee, *Phys. Rev. B* **2005**, *71*, 075307.
18 P. L. Holland, *Acc. Chem. Res.* **2015**, *48*, 1696.
19 R. Poli, J. N. Harvey, *Chem. Soc. Rev.* **2003**, *32*, 1.
20 J. N. Harvey, *Phys. Chem. Chem. Phys.* **2007**, *9*, 331.
21 D. Schröder, D. Shaik, H. Schwarz, *Acc. Chem. Res.* **2000**, 33, 139–145.
22 L. A. Keeling, L. Chen, C. M. Greenlief, A. Mahajan, D. Bonser, *Chem. Phys. Lett.* **1994**, *217*, 136.
23 D.-A. Klug, C. M. Greenlief, *J. Vac. Sci. Technol. A* **1996**, *14*, 1826.
24 K. M. Bulanin, A. G. Shah, A. V. Teplyakov, *J. Chem. Phys.* **2001**, *115*, 7187.
25 M. Kiskinova, J. T. Yates, Jr., *Surf. Sci.* **1995**, *325*, 1.
26 M. J. Dresser, P. A. Taylor, R. M. Wallace, W. J. Choyke, J. T. Yates, Jr., *Surf. Sci.* **1989**, *218*, 75.
27 M. C. Flowers, N. B. H. Jonathan, A. Morris, S. Wright, *Surf. Sci.* **1996**, *351*, 87.
28 S. F. Bent, *Surf. Sci.* **2002**, *500*, 879.
29 J. Yoshinobu, *Prog. Surf. Sci.* **2004**, *77*, 37.
30 A. D. Becke, *J. Chem. Phys.* **1993**, *98*, 5648.
31 P. J. Stephens, F. J. Devlin, C. F. Chabalowski, M. J. Frish, *J. Phys. Chem.* **1994**, *98*, 11623.
32 R. H. Hertwig, W. Koch, *Chem. Phys. Lett.* **1997**, *268*, 345.
33 F. Weigend, R. Ahlrichs, *Phys. Chem. Chem. Phys.* **2005**, *7*, 3297.
34 F. Weigend, *Phys. Chem. Chem. Phys.* **2006**, *22*, 1057.
35 C. Møller, M. S. Plesset, *Phys. Rev.* **1934**, *46*, 618.
36 M. W. Schmidt, K. K. Baldridge, J. A. Boatz, S. T. Elbert, M. S. Gordon, J. H. Jensen, S. Koseki, N. Matsunaga, K. A. Nguyen, S. Su, T. L. Windus, M. Dupuis, J. A. Montgomery, Jr., *J. Comput. Chem.* **1993**, *14*, 1347.
37 L. Clemen, R. M. Wallace, P. A. Taylor, M. J. Dresser, W. J.

Choyke, W. H. Weinberg, J. T. Yates, Jr., *Surf. Sci.* **1992**, *268*, 205.
38 P. A. Redhead, *Vacuum* **1962**, *12*, 203.
39 T. Lim, J. C. Polanyi, H. Guo, W. Ji, *Nat. Chem.* **2010**, *3*, 85.
40 T. B. Lim, I. R. McNab, J. C. Polanyi, H. Guo, W. Ji, *J. Am. Chem. Soc.* **2011**, *133*, 11534.
41 J. Wang, D. Y. Zubarev, M. R. Philpott, S. Vukovic, W. A. Lester, T. Cui, Y. Kawazoe, *Phys. Chem. Chem. Phys.* **2010**, *12*, 9839.
42 D. Cho, K. C. Ko, H. Park, J. Y. Lee, *J. Phys. Chem. C* **2015**, *119*, 10109.
43 K. Tada, H. Koga, Y. Ato, A. Hayashi, M. Okumura, S. Tanaka, *Mol. Phys.* **2019**, *117*, 2251.
44 K. Tada, T. Maruyama, H. Koga, M. Okumura, S. Tanaka, *Molecules* **2019**, *24*, 505.
45 R. Petuya, A. Arnau, *Carbon* **2017**, *116*, 599.
46 L. Noodleman, T. Levell, W.-G. Han, J. Li, F. Himo, *Chem. Rev.* **2004**, *104*, 459.
47 K. Yamaguchi, T. Kawakami, Y. Takano, Y. Kitagawa, Y. Yamashita, H. Fujita, *Int. J. Quant. Chem.* **2002**, *90*, 370.
48 Y. Jung, Y. Shao, M. S. Gordon, D. J. Doren, M. Head-Gordon, *J. Chem. Phys.* **2003**, *119*, 10917.
49 A. O. Lykhin, D. S. Kaliakin, G. E. dePolo, A. A. Kuzubov, S. A. Varganov, *Int. J. Quantum Chem.* **2016**, *116*, 750.
50 G. Granucci, M. Persico, G. Spighi, *J. Chem. Phys.* **2012**, *137*, 22A501.
51 H. Nakano, *Chem. Phys. Lett.* **1993**, *207*, 372.
52 H. Nakano, *J. Chem. Phys.* **1993**, *99*, 7983.
53 B. O. Roos, M. Szulkin, M. Jaszuński, *Theor. Chim. Acta* **1987**, *71*, 375.
54 J. Ivanic, K. Ruedenberg, *Theor. Chem. Acc.* **2001**, *106*, 339.
55 A. O. Lykhin, S. A. Varganov, *Phys. Chem. Chem. Phys.* **2020**, *22*, 5500.
56 D. A. Fedorov, S. E. Pruitt, K. Keipert, M. S. Gordon, S. A. Varganov, *J. Phys. Chem. A* **2016**, *120*, 2911.
57 D. A. Fedorov, A. O. Lykhin, S. A. Varganov, *J. Phys. Chem. A* **2018**, *122*, 3480.
58 R. R. Zaari, S. A. Varganov, *J. Phys. Chem. A* **2015**, *119*, 1332.
59 T. Takayanagi, Y. Watabe, T. Miyazaki, *Molecules* **2020**, *25*, 882.